Conformal Perfectly Matched Layer for the Mixed Finite Element Time-Domain Method

Burkay Donderici and Fernando L. Teixeira, *Senior Member, IEEE*

***Abstract*—We introduce a conformal perfectly matched layer (PML) for the finite-element time-domain (FETD) solution of transient Maxwell equations in open domains. The conformal PML is implemented in a mixed FETD setting based on a direct discretization of the first-order coupled Maxwell curl equations (as opposed to the second-order vector wave equation) that employs edge elements (Whitney 1-form) to expand the electric field and face elements (Whitney 2-form) to expand the magnetic field. We show that the conformal PML can be easily incorporated into the mixed FETD algorithm by utilizing PML constitutive tensors whose discretization is naturally decoupled from that of Maxwell curl equations (spatial derivatives). Compared to the conventional (rectangular) PML, a conformal PML allows for a considerable reduction on the amount of buffer space in the computational domain around the scatterer(s).**

***Index Terms*—Finite-element time-domain (FETD) method, perfectly matched layers (PMLs).**

I. Introduction

THE finite-element time-domain (FETD) method has been widely employed for the solution of transient Maxwell equations in complex geometries [1]–[12]. Compared with time-domain methods based on regular structured grids such as finite-difference time-domain (FDTD), FETD has more geometrical flexibility because it can be based upon simplicial grids. The main drawback of FETD compared to FDTD is the need to solve a sparse linear system at each time step.

A. Mixed FETD Versus Second-Order Wave Equation FETD

There are two main approaches to construct FETD schemes for Maxwell equations. The first approach is based on the discretization of the second-order vector wave equation [1]–[3]. In this case, either the electric or the magnetic field is the sole unknown and only one type of basis function (that may include high order versions) is employed. Edge elements are typically used as the basis functions of choice for the electric field because they conform to a discrete version of the de Rham diagram [13] and avoid the presence of spurious modes at non-zero frequencies. The second approach to construct FETD for Maxwell equations is based on the discretization of the two coupled first-order Maxwell curl equations [5]–[15]. In this case, the electric field and the magnetic field are the simultaneous unknowns of the problem and a mixed set of basis functions is used. In particular, a mixed $E-B$ FETD algorithm is discussed in [7], [10]–[12]. This algorithm uses edge elements (Whitney 1-form) to expand the electric field and face elements (Whitney 2-form) to expand the magnetic field, and employ discrete Galerkin Hodge operators [12], [16] as mass matrices. Among the desirable characteristics of this mixed $E-B$ FETD are: (*i*) It retains conformality to the discrete de Rham diagram; (*ii*) it does not admit spurious solutions of the form $t\nabla\phi$ (which are present in the second-order wave equation FETD [5], [17], [18]); (*iii*) it leads to symplectic (energy-conserving) schemes under leap-frog time discretization [19]; (*iv*) it provides a natural path for hybridization with FDTD since the latter can be likewise developed using a mix of edge/face elements [20]; and (*v*) it is easily extended to frequency dispersive or anisotropic media because these properties can be incorporated into separate steps in the time-update that do not involving spatial derivatives [21].

Even though the mixed $E-B$ FETD utilizes two fields as unknowns, its computational cost is comparable to the second-order wave equation FETD formulation. This is because the sparse linear system solution is only required for the electric field update in the mixed FETD, with the update of the magnetic field being "matrix-free" (explicit). As a result, the size of the linear system to be solved at each time step is the same as in the second-order wave equation FETD formulation. Moreover, the mixed FETD involves only first-order time derivatives and hence only one past time-step electric/magnetic field value is necessary for the time update (using a conventional leap-frog time discretization). In contrast, time-discretization of the second-order time derivative necessitates storage of *two* previous time-step values.

B. PML for FETD

Absorbing boundary conditions are routinely employed in FDTD and FETD simulations of open-domain problems in order to avoid spurious reflections from the grid terminations. The perfectly matched layer (PML) in particular has become a very popular absorbing boundary condition because of its efficacy and ease of implementation, and because it preserves the underlying sparsity of the methods. The PML was originally developed for rectangular FDTD grids (Cartesian PML) [22]–[27] and later implemented in rectangular FETD grid terminations [17], [28]–[30].

C. Conformal PML

The original PML concept applied only to Cartesian coordinates (planar interfaces). To extend its range of applicability, the PML concept was implemented in nonorthogonal FDTD

Manuscript received August 13, 2007; revised November 20, 2007. This work was supported in part by the AFOSR under MURI Grant FA 9550-04-1-0359, the NSF under CAREER Grant ECCS-0347502, and in part by the OSC under Grants PAS-0061 and PAS-0110.

The authors are with the ElectroScience Laboratory and Department of Electrical and Computer Engineering, The Ohio State University, Columbus, OH 43212 USA (e-mail: donderici.1@osu.edu; teixeira@ece.osu.edu).

Digital Object Identifier 10.1109/TAP.2008.919215

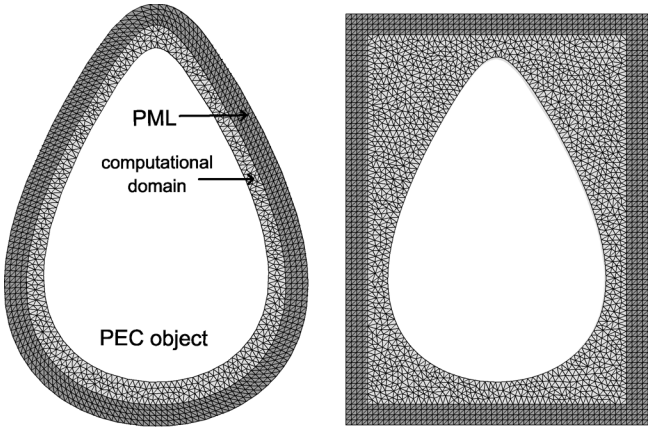

(a) conformal PML (b) rectangular PML

Fig. 1. A conformal PML (left) can greatly reduce the amount of buffer space around the scatterer compared to the Cartesian PML (right).

grids and curvilinear FEM meshes with good results [31]–[33]. However, these implementations were based on an *approximate* matching because they assumed of the metric coefficients to be independent of the spatial coordinates, which is not true in curvilinear coordinates. Later, true PMLs—in the sense of providing reflectionless absorption in the continuum limit—were derived for cylindrical and spherical mesh terminations in [34]–[38]. and, more generally, for conformal mesh terminations in [39], [40] based on a complex stretching (analytic continuation) of the normal coordinate to the mesh termination [41].

A conformal PML is of interest because it can be placed on the convex hull enclosing the scatterer(s) to reduce the amount of buffer space in the computational domain. The savings in memory can be considerable, especially in problems involving impenetrable scatterer(s), as illustrated in Fig. 1. The conformal PML can be expressed in terms of dispersive and anisotropic constitutive tensors that depend on the *local* principal radii of curvature of the mesh termination surface [39]. Implementations of the conformal PML have been considered in non-staggered body-fitted FDTD grids [42], [43], frequency-domain finite element simulations [44]–[47], and FETD simulations [48], the latter being restricted to the second-order wave equation FETD formulation.

D. Objectives and Outline

In this paper, we develop a conformal PML implementation for the mixed $E-B$ FETD algorithm. As alluded above, the mixed FETD algorithm provides a simple and natural route to incorporate the dispersive and anisotropic tensors that comprise the conformal PML since the update of the constitutive equations is derived and implemented separately from the update of Maxwell curl equations. Indeed, in the mixed FETD, the conformal PML implementation boils down to a modification in the calculation of the two Hodge (mass) matrices $[\star_\epsilon]$ and $[\star_{\mu^{-1}}]$.

The proposed conformal PML-FETD formulation is tested in a number of examples involving transient field scattering from both impenetrable (PEC) and penetrable (dispersive media) objects, to verify its efficacy. The late-time stability of the conformal PML and the energy conservation properties of the underlying FETD are also verified numerically.

II. Mixed E-B FETD: Basic Formulation

In the mixed $E-B$ FETD, the electric field intensity $\vec{E}$ and the magnetic field flux density $\vec{B}$ are expanded in terms of Whitney edge elements $\vec{W}_i^1$, $i=1,\ldots,N_e$, and Whitney face elements $\vec{W}_i^2$, $i=1,\ldots,N_f$, respectively, as follows:

$$\vec{E}=\sum_{i=1}^{N_e} e_i\vec{W}_i^1 \quad \vec{B}=\sum_{i=1}^{N_f} b_i\vec{W}_i^2 \tag{1}$$

where e_i and b_i are the unknown expansion coefficients or degrees of freedom (DoFs) of the problem, N_e is the number of interior (free) edges in the problem, and N_f is the number of faces, respectively. If we define column vectors of DoFs as $\mathbb{E}=[e_1,e_2,\ldots,e_{N_e}]^T$ and $\mathbb{B}=[b_1,b_2,\ldots,b_{N_f}]^T$, where the superscript denotes transpose, the semi-discrete Maxwell equations can be written as [14], [49]

$$[\star_\epsilon]\frac{\partial}{\partial t}\mathbb{E}=[\mathcal{D}^*_{\text{curl}}]\,[\star_{\mu^{-1}}]\mathbb{B}-\mathbb{J}_s \tag{2}$$

$$\frac{\partial}{\partial t}\mathbb{B}=-[\mathcal{D}_{\text{curl}}]\mathbb{E}-\mathbb{M}_s \tag{3}$$

where the $N_f\times N_e$ matrix $[\mathcal{D}_{\text{curl}}]$ and the $N_e\times N_f$ matrix $[\mathcal{D}^*_{\text{curl}}]$ are *curl incidence matrices* (discrete analogues of the exterior derivative d acting on 1-forms) on the primal and dual grids, respectively [49], [50]). The primal grid is chosen as the finite element mesh itself. Both $[\mathcal{D}_{\text{curl}}]$ and $[\mathcal{D}^*_{\text{curl}}]$ are metric-free matrices whose elements assume only $\{-1,0,1\}$ values [15], [49], [50]. Assuming homogeneous Dirichlet boundary conditions, we have $[\mathcal{D}^*_{\text{curl}}]=[\mathcal{D}_{\text{curl}}]^T$ [50]. The column vectors $\mathbb{J}_s=[\mathrm{j}_1,\mathrm{j}_2,\ldots,\mathrm{j}_{N_e}]^T$ and $\mathbb{M}_s=[\mathrm{m}_1,\mathrm{m}_2,\ldots,\mathrm{m}_{N_f}]^T$ represent (known) electric and magnetic source current densities, respectively. The column vector $\mathbb{M}_s$ is associated with faces of the primal (finite-element) mesh, while $\mathbb{J}_s$ is associated with faces of the dual mesh [49]. The $N_e\times N_e$ matrix $[\star_\epsilon]$ and the $N_f\times N_f$ matrix $[\star_{\mu^{-1}}]$ represent discrete Hodge star operators, an isomorphism between primal grid variables and dual grid variables that incorporate all metric information of the mesh [12], [14]–[16], [49], [50]. In the finite element literature, these matrices are commonly referred as *mass* matrices.

Using a leap-frog time discretization in (2) and (3), the FETD update equations in lossless, nondispersive media can be written as

$$[\star_\epsilon]\mathbb{E}^{n+1}=[\star_\epsilon]\mathbb{E}^n+\Delta t[\mathcal{D}_{\text{curl}}]^T[\star_{\mu^{-1}}]\mathbb{B}^{n+\frac{1}{2}}-\Delta t\mathbb{J}_s^{n+\frac{1}{2}} \tag{4}$$

$$\mathbb{B}^{n+\frac{1}{2}}=\mathbb{B}^{n-\frac{1}{2}}-\Delta t[\mathcal{D}_{\text{curl}}]\mathbb{E}^n-\Delta t\mathbb{M}_s^n \tag{5}$$

The solution for $\mathbb{E}$ and $\mathbb{B}$ at each time step can be obtained by either solving a sparse linear system for $\mathbb{E}$ for each n. or by constructing a sparse approximate matrix inverse $[\star_\epsilon]^{-1}$ [15]. Since $[\star_\epsilon]$ is sparse and SPD, the linear solve can be done efficiently using direct (for small- and moderate-size problems) or iterative (for large-scale problems) solvers. The above update equations are similar to the leap-frog update equations in FDTD, expect for the fact that in the latter case, $[\star_\epsilon]$ is diagonal and the inversion is trivial.

If we denote i and j as the row and column indices respectively, the (Galerkin) Hodge matrices are given by the following integrals

$$[\star_\epsilon]_{ij} = \int_\Omega \vec{W}_i^1 \cdot \bar{\bar{\epsilon}}(\vec{r}) \cdot \vec{W}_j^1 d\Omega \tag{6}$$

$$[\star_{\mu^{-1}}]_{ij} = \int_\Omega \vec{W}_i^2 \cdot \bar{\bar{\mu}}^{-1}(\vec{r}) \cdot \vec{W}_j^2 d\Omega \tag{7}$$

where Ω is the computation domain, and $\bar{\bar{\epsilon}}(\vec{r})$ and $\bar{\bar{\mu}}(\vec{r})$ are permittivity and permeability tensors, respectively. In 3-D, (6) and (7) are volume integrals.

In the 2-D TE_z cases considered in what follows, (6) and (7) become area integrals, while E and B are still a 1-form and a 2-form, respectively. As a result, all the above formulas still apply using the proper definitions for the two-dimensional $\vec{W}_i^1$ and $\vec{W}_i^2$ [16].[1] On the other hand, in the 2-D TM_z case (not considered here), E is a 0-form and hence it should be expanded instead by nodal or "grad-conforming" elements (Whitney 0-forms), while B is a 1-form and hence it should be expanded by curl-conforming edge elements. A discussion on the proper choice of basis functions to expand each of the fields in various dimensions and polarizations is given in [16]. Moreover, a complete classification table for the differential forms representing each field (associated with the proper choice of basis functions) is presented in [15].

III. Conformal PML-FETD Formulation

The permittivity and permeability tensors of the conformal PML in the TE_z case are given in terms of the stretching variables $\gamma(\rho)$ and $s(\rho)$ in local coordinates indicated in Fig. 2 as follows [39], [42]:

$$\begin{aligned} \bar{\bar{\epsilon}}(\vec{r}) &= \bar{\bar{\epsilon}}(\rho) = \hat{\rho}\hat{\rho}\frac{\gamma(\rho)}{s(\rho)} + \hat{\varphi}\hat{\varphi}\frac{s(\rho)}{\gamma(\rho)} \\ \bar{\bar{\mu}}(\vec{r}) &= \bar{\bar{\mu}}(\rho) = \hat{z}\hat{z}\gamma(\rho)s(\rho) \end{aligned} \tag{8}$$

where

$$\gamma(\rho) = \frac{1}{\rho}\left(\rho_0 + \int_{\rho_0}^{\rho_0+l} s(\rho)d\rho\right) = \kappa(\rho) + \frac{\sigma_\varphi(\rho)}{\jmath\omega\epsilon_0} \tag{9}$$

$$s(\rho) = 1 + \frac{\sigma_\rho(\rho)}{\jmath\omega\epsilon_0}. \tag{10}$$

A local (z-invariant) orthogonal Darboux frame [39] with unit vectors $\hat{\rho}$, $\hat{\varphi}$, and $\hat{z}$ is utilized in (8)–(10). This is *locally* equivalent to a cylindrical coordinate system with the origin located at the (local) center of curvature of each point M along the PML interface [39], cf. Fig. 2.

In 2-D, a *face-based* discretization for the PML tensors is used with $\bar{\bar{\epsilon}}(\rho)$ indexed as $\bar{\bar{\epsilon}}(k)$ and $\bar{\bar{\mu}}(\rho)$ indexed as $\bar{\bar{\mu}}(k)$, where k is the face index. The PML parameters can be similarly indexed as $\gamma(k)$, $s(k)$, $\sigma_\rho(k)$, $\sigma_\varphi(k)$, and $\kappa(k)$.

[1]For example, the Whitney form $\vec{W}_i^2$ is a z-directed vector function that is uniform over each face, representing a 2-D 'volume' form [16].

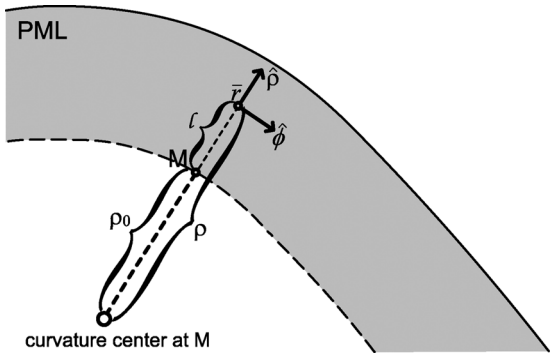

Fig. 2. Conformal PML geometry and parametrization. The point $\vec{r}$ along the radial direction inside the PML is given in terms of the local coordinate ρ as $\vec{r} = \rho\hat{\rho} = (\rho_0 + l)\hat{\rho}$, as illustrated. Note that the coordinate system depicted here is a local one, with the (local) radius of curvature ρ_0 at the free-space/PML boundary being a function of the point M along the PML interface [39].

A. Electric Field Update

In order to obtain the electric field update, a set of algebraic manipulations are performed on the Hodge matrix $[\star_\epsilon]$. If we denote face k as Ω_k, the domain of integration in (6) can be decomposed as a sum over the Ω_k's so that

$$[\star_\epsilon]_{ij} = \sum_{k=1}^{N_f} \int_{\Omega_k} \vec{W}_i^1 \cdot \bar{\bar{\epsilon}}(k) \cdot \vec{W}_j^1 d\Omega. \tag{11}$$

Substituting (8) in (11) and separating components yields

$$[\star_\epsilon] = \sum_{k=1}^{N_f} \frac{\gamma(k)}{s(k)} [\mathcal{L}_\rho(k)] + \sum_{k=1}^{N_f} \frac{s(k)}{\gamma(k)} [\mathcal{L}_\varphi(k)] \tag{12}$$

with $[\mathcal{L}_\rho(k)]_{ij}$ given by

$$[\mathcal{L}_\rho(k)]_{ij} = \int_{\Omega_k} \left(\hat{\rho}\cdot\vec{W}_i^1\right)\left(\hat{\rho}\cdot\vec{W}_j^1\right) d\Omega \tag{13}$$

and similarly for $[\mathcal{L}_\varphi(k)]_{ij}$. A further simplification can be performed by considering the Hodge matrix-vector multiplication in (4) and defining an electric flux density vector[2] $\mathbb{D} = [\star_\epsilon]\mathbb{E}$. Substituting (12) in this definition for $\mathbb{D}$, we get

$$\mathbb{D} = \sum_{k=1}^{N_f} \frac{\gamma(k)}{s(k)} [\mathcal{L}_\rho(k)]\,\mathbb{E} + \sum_{k=1}^{N_f} \frac{s(k)}{\gamma(k)} [\mathcal{L}_\varphi(k)]\,\mathbb{E}. \tag{14}$$

Although the above summations run over all faces, the inner-products $[\mathcal{L}_\rho(k)]$ and $[\mathcal{L}_\varphi(k)]$ produce non-zero values only for two faces per edge. If we denote these faces as $k_{\downarrow j}$ and $k_{\uparrow j}$ for each edge j, and denote $\mathbb{D} = [d_1, d_2, \ldots, d_{N_f}]^T$, the summation above can be rewritten as

$$\begin{aligned} d_j = &\sum_{i=1}^{N_e} \frac{\gamma(k_{\uparrow j})}{s(k_{\uparrow j})} [\mathcal{L}_\rho(k_{\uparrow j})]_{ij}\, e_i + \sum_{i=1}^{N_e} \frac{\gamma(k_{\downarrow j})}{s(k_{\downarrow j})} [\mathcal{L}_\rho(k_{\downarrow j})]_{ij}\, e_i \\ &+ \sum_{i=1}^{N_e} \frac{s(k_{\uparrow j})}{\gamma(k_{\uparrow j})} [\mathcal{L}_\varphi(k_{\uparrow j})]_{ij}\, e_i + \sum_{i=1}^{N_e} \frac{s(k_{\downarrow j})}{\gamma(k_{\downarrow j})} [\mathcal{L}_\varphi(k_{\downarrow j})]_{ij}\, e_i. \end{aligned} \tag{15}$$

[2]Note that, inside the PML, the electric flux density defined in this manner incorporates PML stretching variables.

Each term in (15) can be considered separately, by taking the stretching variables out of the summation and writing

$$d_j = d_{\rho\uparrow j} + d_{\rho\downarrow j} + d_{\varphi\uparrow j} + d_{\varphi\downarrow j} \tag{16}$$

where

$$d_{\rho\uparrow j} = \frac{\gamma(k_{\uparrow j})}{s(k_{\uparrow j})} e_{\rho\uparrow j} \tag{17}$$

and

$$e_{\rho\uparrow j} = \sum_{i=1}^{N_e} [\mathcal{L}_\rho(k_{\uparrow j})]_{ij}\, e_i \tag{18}$$

and similarly for $d_{\rho\downarrow j}$, $d_{\varphi\uparrow j}$, $d_{\varphi\downarrow j}$, $e_{\rho\downarrow j}$, $e_{\varphi\uparrow j}$, and $e_{\varphi\downarrow j}$, with $j = 1, \ldots, N_e$. Note that four different equations per edge need to be considered because each edge touches two faces and each face possibly has two different frequency dependencies (along φ and ρ). Substituting (9) and (10) into (17) and rearranging terms, $d_{\rho\uparrow j}$ and $e_{\rho\uparrow j}$ can be related through

$$d_{\rho\uparrow j} = \frac{\sigma_\varphi(k) + \jmath\omega\epsilon_0\kappa(k)}{\sigma_\rho(k) + \jmath\omega\epsilon_0} e_{\rho\uparrow j}. \tag{19}$$

The time-domain discretization of (19) is inverse Fourier transforming and approximating time derivatives using central differences with time step Δt. The resulting update equation is given by

$$\begin{aligned} d_{\rho\uparrow j}|^{n+1} = &\left(\frac{\sigma_\varphi(k_{\uparrow j})\Delta t + 2\epsilon_0\kappa(k_{\uparrow j})}{\sigma_\rho(k_{\uparrow j})\Delta t + 2\epsilon_0}\right) e_{\rho\uparrow j}|^{n+1} \\ &+ \left(\frac{\sigma_\varphi(k_{\uparrow j})\Delta t - 2\epsilon_0\kappa(k_{\uparrow j})}{\sigma_\rho(k_{\uparrow j})\Delta t + 2\epsilon_0}\right) e_{\rho\uparrow j}|^{n} \\ &- \left(\frac{\sigma_\rho(k_{\uparrow j})\Delta t - 2\epsilon_0}{\sigma_\rho(k_{\uparrow j})\Delta t + 2\epsilon_0}\right) d_{\rho\uparrow j}|^{n} \end{aligned} \tag{20}$$

and similarly for $d_{\rho\downarrow i}$, $d_{\varphi\uparrow i}$, $d_{\varphi\downarrow i}$. If we denote the factor multiplying $e_{\rho\uparrow j}|^{n+1}$ in the above equation as $w_\rho(k_{\uparrow j})$ and the overall contribution from the (known) past time step field values as $g_{\rho\uparrow j}|^n$, (20) can be written more compactly as

$$d_{\rho\uparrow j}|^{n+1} = w_\rho(k_{\uparrow j}) e_{\rho\uparrow j}|^{n+1} + g_{\rho\uparrow j}|^n. \tag{21}$$

Substituting (18), (21), and the corresponding expressions for $d_{\rho\downarrow i}$, $d_{\varphi\uparrow i}$, $d_{\varphi\downarrow i}$ in (16), and writing the result in a matrix form, we obtain

$$[\mathcal{A}]\mathbb{E}^{n+1} = \mathbb{D}^{n+1} - \mathbb{G}^n \tag{22}$$

where

$$[\mathcal{A}] = [\mathcal{W}_{\rho\uparrow}][\mathcal{L}_{\rho\uparrow}] + [\mathcal{W}_{\rho\downarrow}][\mathcal{L}_{\rho\downarrow}] + [\mathcal{W}_{\varphi\uparrow}][\mathcal{L}_{\varphi\uparrow}] + [\mathcal{W}_{\varphi\downarrow}][\mathcal{L}_{\varphi\downarrow}] \tag{23}$$

with $[\mathcal{W}_{\rho\uparrow}] = \mathrm{diag}\{w_\rho(k_{\uparrow 1}), w_\rho(k_{\uparrow 2}), \ldots, w_\rho(k_{\uparrow N_e})\}$ and similarly for $[\mathcal{W}_{\rho\downarrow}]$, $[\mathcal{W}_{\varphi\uparrow}]$, $[\mathcal{W}_{\varphi\downarrow}]$, and $\mathbb{G} = [g_1, g_2 \ldots, g_{N_e}]^T$ with $g_j = g_{\rho\uparrow j} + g_{\rho\downarrow j} + g_{\varphi\uparrow j} + g_{\varphi\downarrow j}$.

B. Magnetic Field Update

The magnetic field update can be derived along similar lines as the electric field update. The final update equation for the magnetic field is written in matrix form as

$$[\mathcal{A}_\mu]\mathbb{H}^{n+\frac{1}{2}} = \mathbb{B}^{n+\frac{1}{2}} - \mathbb{G}_\mu^{n-\frac{1}{2}} \tag{24}$$

where $[\mathcal{A}_\mu]$ and $\mathbb{G}_\mu^n$ are analogous to $[\mathcal{A}]$ and $\mathbb{G}^n$ respectively. The column vector $\mathbb{H} = [\star_{\mu^{-1}}]\mathbb{B}$ represents magnetic field intensity. The matrix $[\mathcal{A}_\mu]$ is defined as the diagonal matrix given by the matrix product

$$[\mathcal{A}_\mu] = [\mathcal{W}_z][\mathcal{L}_z] \tag{25}$$

where $[\mathcal{L}_z]$ and $[\mathcal{W}_z]$ are both diagonal matrices representing inner-product and coefficient matrices analogous to $[\mathcal{L}_\rho]_{ij}$ and $[\mathcal{W}_\rho]$, respectively. Since $[\mathcal{A}_\mu]$ is diagonal (explicit update), no linear solve is required in the magnetic update.

C. Curl Equations and Full Update

The update equations for $\mathbb{D}$ and $\mathbb{B}$ are explicit and can be obtained directly from a leap-frog time discretization of (2) and (3) with $\mathbb{D} = [\star_\epsilon]\mathbb{E}$ as

$$\mathbb{D}^{n+1} = \mathbb{D}^n + \Delta t[\mathcal{D}_{\mathrm{curl}}]^T\mathbb{H}^{n+\frac{1}{2}} - \Delta t\mathbb{J}_s^{n+\frac{1}{2}} \tag{26}$$

$$\mathbb{B}^{n+\frac{1}{2}} = \mathbb{B}^{n-\frac{1}{2}} - \Delta t[\mathcal{D}_{\mathrm{curl}}]\mathbb{E}^n - \Delta t\mathbb{M}_s^n. \tag{27}$$

A complete time step update for the electromagnetic fields consists of applying (27), (24), (26), and (22) in sequence.

For the 3-D implementation, two basic changes are necessary in the development above. First, the tensor in (8) should be replaced by the more general tensor derived in [39], in terms of the *two* principal radii of curvature of a general (doubly-curved) surface. This would produce three terms, instead of two in (24) and (14). Second, since an edge contacts more than two faces in 3-D, extra terms would appear in (15).

IV. Results

The accuracy of the proposed PML-FETD is examined via several test cases. Unless specified otherwise, the common parameters used in the following examples are as follows. TE_z problems are considered in 2-D with an magnetic point source excited by an ultra-wideband (UWB) time-domain excitation of the form $f(t) = -0.488\sin(2t\pi v_c/\lambda_0) + 0.290\sin(4t\pi v_c/\lambda_0) - 0.031\sin(6\pi v_c/\lambda_0)$ for $0 < t < \lambda_0/v_c$ and $f(t) = 0$ otherwise (a Blackman-Harris pulse derivative), where v_c is the speed of light. The central wavelength in free space is $\lambda_0 = 0.6$ m, which corresponds to a central frequency of 500 MHz. The time step is chosen according to the length of the shortest edge l_{min} and is given by $\Delta t = c_N l_{min}/v_c$, with Courant number $c_N = 0.2$. A mesh generation algorithm with a maximum face element area constraint $\Omega_k < \sqrt{3}l_e^2/4$ for all faces $k = 1, \ldots, N_f$, is used, where l_e is the resolution of the mesh in terms of an edge length. A sparse incomplete Cholesky factorization with a drop tolerance value 10^{-10} is

used to solve (22). The shape of the PML boundary is described by analytical functions, while the radius of curvature required in the calculation of the conformal PML parameters is calculated numerically using a set of grid points much denser than the finite-element nodes. This implies that the error in the (numerical) calculation of the local radius of curvature is negligible vis-à-vis other sources of error. A polynomial profile of order $m = 2.5$ is used for the PML stretching variable $s(\rho)$. The maximum value of the PML conductivity profile is determined by the standard criterion used for FDTD [51]. This criterion may not be optimal for FETD, but a detailed study on the optimal PML conductivity profile for FETD is beyond the objectives here.

A. Scattering From a PEC Circular Cylinder

In this Section, the scattered field from a PEC circular cylinder is calculated using the conformal PML-FETD and compared against both FDTD and analytical results. The center of the cylinder is located at $(x_o, y_o) = (0.4, 0.4)$ m and the cylinder has a radius $R = 0.34$ m. An average edge length of $\lambda/60 = 1$ cm is used for the finite element mesh, which is shown in Fig. 3(a). The source is located at $(x_s, y_s) = (0.96, 0.45)$ m and the magnetic field is probed at $(x_p, y_p) = (0.96, 0.35)$ m. The scattered field is given by $s_{k_p}|^n = h^c_{k_p}|^n - h^f_{k_p}|^n$, where $h^c_{k_p}|^n$ is the magnetic field calculated with circular cylinder present and $h^f_{k_p}|^n$ is the magnetic field calculated in free-space. The number of (rectangular) faces in the reference FDTD simulation is chosen the same as the number of faces in the FETD simulation. A staircase approximation is used to model the circular cylinder in FDTD.

The analytical solution is obtained from the Green's function for this problem, which is expressed in terms of a Hankel-Bessel series over the azimuth index [52, pp. 574–667], with the first 50 terms included. The time-domain source excitation is first converted to frequency-domain by a Fourier transformation. The frequency resolution is increased by zero padding with a length that is 10 times the total number of time steps. The source spectrum, at each frequency, is multiplied by the analytical solution at that frequency. The final time-domain result is obtained by an inverse Fourier transformation.

Fig. 3(b) shows that the scattered field obtained by the conformal PML-FETD agrees very well with both FDTD and analytical results. The normalized residual error in FETD is calculated as

$$\delta(n) = 20\log_{10}\left(\frac{\left|s^{\text{fetd}}_{k_p}|^n - s^{\text{analytic}}_{k_p}|^n\right|}{\max_n\left|s^{\text{analytic}}_{k_p}|^n\right|}\right) \qquad (28)$$

and similarly for FDTD. The residual error is shown in Fig. 3(c). It is seen that the error in the FDTD result is larger than the FETD error for the resolution considered, with peak levels of -44 dB and -28 dB for FETD and FDTD, respectively. This is despite the fact that the edge length in the FDTD grid is smaller than the average edge length of the FETD grid (0.77 cm versus 1.00 cm).

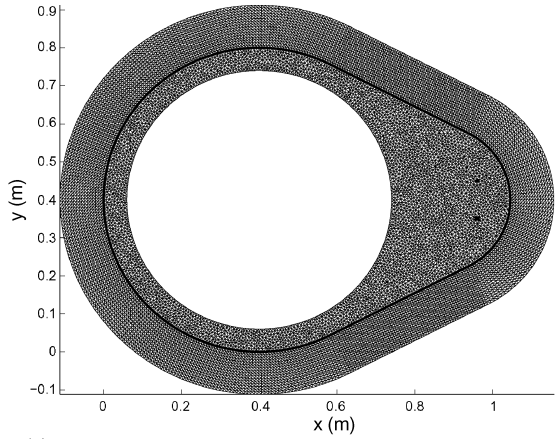

(a) Mesh used for a point source nearby a circular PEC cylinder.

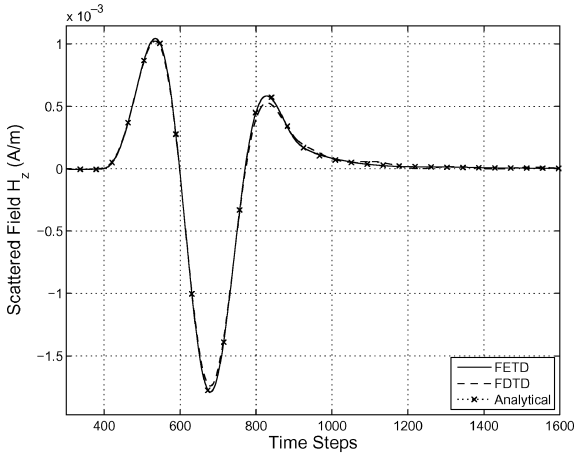

(b) Time-domain scattered fields.

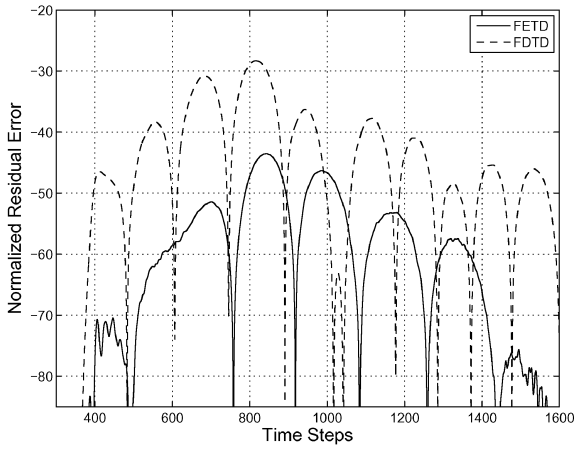

(c) Normalized residual errors.

Fig. 3. Scattered field and normalized residual error for a point source illuminating a circular PEC cylinder. (a) The finite element mesh comprises 33,487 edges and 22,046 faces. The source and the probe location are located at the right of the scatterer, indicated by small + and × symbols, respectively. (b) The time-domain response of the conformal PML-FETD method and the FDTD method agree very well with the analytical result. (c) Due to staircasing approximations, the error in the FDTD result is on average about 10 dB larger than the error in the FETD result for the mesh considered.

B. Conformal PML: Reflection Error

The accuracy of the proposed conformal PML is further demonstrated by calculating reflection errors using different number of layers N_{PML} in the PML region. In this case, an

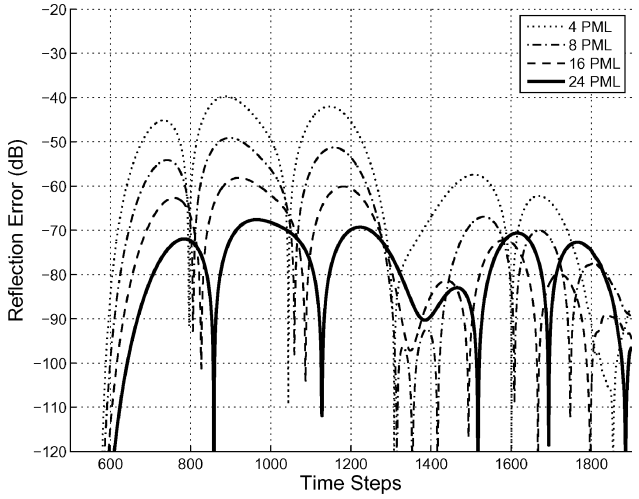

(a) PML reflection error vs. time.

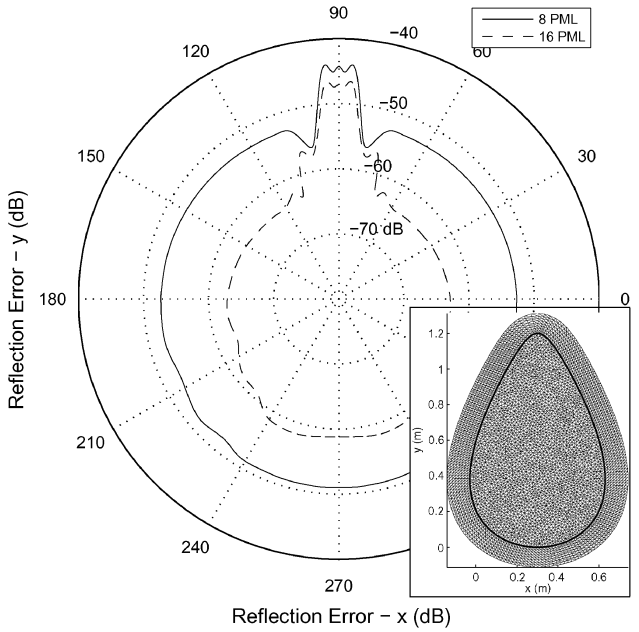

(b) PML reflection error vs. position along PML boundary.

Fig. 4. Reflection error versus (a) time and (b) position along the PML boundary, for various $N_{\rm PML}$: (a) The PML reflection levels are progressively reduced for larger $N_{\rm PML}$, with $R = -68$ dB obtained for $N_{\rm PML} = 24$. (b) The PML reflection errors peak at 90°, where the radius of curvature is minimum because a smaller radius reduces the average distance of nearby PML boundary points to the probe location. The finite-element mesh used in this example has 12,748 edges and 8,428 faces.

oval-shaped computational domain with size 0.6×1.2 m^2 is extruded with $N_{\rm PML} = 4$, 8, 16, 24. The finite element mesh for $N_{\rm PML} = 8$ is depicted in the inset of Fig. 4. The average edge length is chosen as $\lambda_0/60 = 1$ cm. The reflection error as a function of time is obtained by placing the point source at $(x_s, y_s) = (0.3, 0.4)$ m and probing the field at $(x_p, y_p) = (0.3, 0.5)$ m. In order to estimate the reflection error as function of position along the conformal PML boundary, the source and probe locations are chosen at different points along the computational domain both at a distance 6 cm away from the PML boundary and 4 cm away from each other. A FETD simulation with the same mesh extruded by an appropriate larger number of *free-space* layers (so that the spurious reflection can be windowed out from the results) is used as reference. The extruded part of the mesh (corresponding to PML or free-space) consists of convex quadrilateral tiles composed of two triangular faces each. These tiles are orthogonal in the Darboux frame local coordinates ρ and φ [39]. A separate reference result consisting of the same mesh terminated by a PEC boundary (and with no extrusion) is used to normalize the reflection coefficient. If we denote the magnetic field values at the probe locations in the simulations with the PML mesh, free-space extruded mesh and the PEC-terminated mesh as $h^{\rm pml}_{k_p}|^n$, $h^f_{k_p}|^n$ and $h^{\rm pec}_{k_p}|^n$, where n is the time step index, the reflection error is calculated as follows:

$$R_{\rm PML}(n) = 20\log_{10}\left(\frac{\left|h^{\rm pml}_{k_p}|^n - h^f_{k_p}|^n\right|}{\max\limits_n \left|h^{\rm pec}_{k_p}|^n - h^f_{k_p}|^n\right|}\right). \quad (29)$$

Fig. 4 shows the reflection errors with respect to time and angular position along the PML boundary for different $N_{\rm PML}$. The angular axis in Fig. 4(b) refers to the location of the source-probe pair in a cylindrical coordinates system centered at $(x_c, y_c) = (0.3, 0.6)$ m. Fig. 4 clearly shows that $R_{\rm PML}$ decreases as $N_{\rm PML}$ is increased with peak reflection levels of -49 dB and -68 dB are observed for $N_{\rm PML} = 8$ and $N_{\rm PML} = 24$, respectively. Fig. 4(b) shows that the reflection errors peaks at 90°. This is because the smaller radius of curvature at that angle reduces the average distance of nearby PML boundary points to the probe location.

The convergence of $R_{\rm PML}$ with respect to $N_{\rm PML}$ is slower in this FETD implementation than what is observed in typical FDTD simulations. The slow convergence of PML in FETD versus FDTD has also been observed elsewhere [17], [21]. Since those papers are based on rectangular PML, it suggests that such feature is related to the finite-element method itself, rather than to conformality aspects. The discretization of the PML conductivity profile is one of the major sources of PML reflection error and one important difference of FETD in this regard is that it does not posses the staggered nature of the FDTD grid. Staggering allows for FDTD to effectively assign twice the number of PML conductivity jumps: one set at electric field locations and the other set at magnetic field locations. This error can be mitigated by using a relatively fine mesh resolution. In this example, we employ on average 60 edges per (central) wavelength. However, there is a fundamental trade-off here because an increase in the mesh resolution—for a given $N_{\rm PML}$—reduces the overall PML thickness and hence the overall attenuation within it.

C. Scattering From Oval PEC Coated With Metamaterial

Although the basic formulation presented in Section II corresponds to free-space, it is easy to extend the mixed $E-B$ FETD to media having inhomogeneous frequency-dependent tensors $\overline{\overline{\epsilon}}(\vec{r},\omega)$ and $\overline{\overline{\mu}}(\vec{r},\omega)$, as detailed in [21].

In this Section, the scattered field from an oval-shaped PEC scatterer coated with a doubly-dispersive isotropic metamaterial layer as shown in Fig. 5(a) is considered. The mesh for this example has average edge lengths of 1 cm and 0.3227 cm in

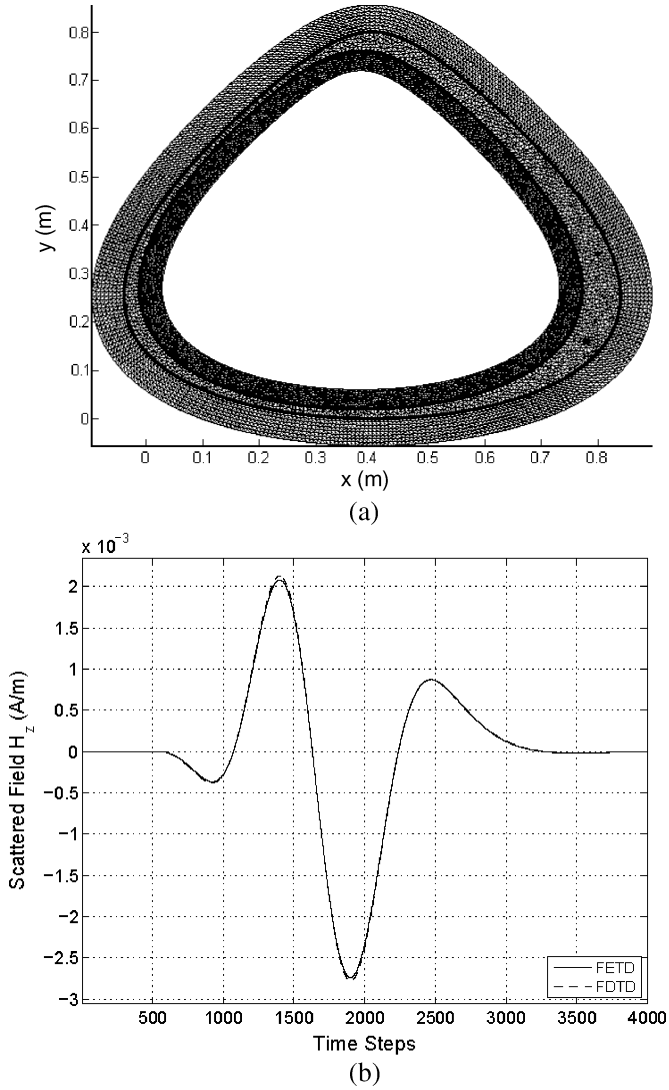

Fig. 5. (a) Finite element mesh for an oval-shaped PEC scatterer coated with a doubly-dispersive material. The mesh has 28,556 edges and 18,741 faces. The source and the probe are located at the right of the scatterer and indicated by small + and × symbols, respectively. A Cartesian PML implementation for this problem would require a mesh about 1.9 times larger. (b) Scattered fields calculated by FETD and FDTD, showing very good agreement.

the free space and metamaterial regions, respectively. The mesh shown in Fig. 5(a) has 28,556 edges and 18,741 faces. This is approximately 1.9 times less than would be required using a Cartesian PML for the same problem. The frequency response of the metamaterial layer is described by a two-species Debye model for both the permittivity and the permeability. The permittivity model writes as

$$\epsilon(\omega) = \epsilon_0\epsilon_\infty + \epsilon_0 \sum_{i=1}^{2} \frac{A_i^\epsilon}{1 + \jmath\omega\tau_p^\epsilon} \tag{30}$$

with parameters given by $\epsilon_\infty = 3.0$, $A_1^\epsilon = 1.45$, $A_2^\epsilon = 0.35$, $\tau_1^\epsilon = 1.5$ nsec, $\tau_2^\epsilon = 0.25$ nsec, and $\sigma = 1.0$ mS/m. The two-species Debye model for the permeability has parameters $\mu_\infty = 1.0$, $A_1^\mu = 0.35$, $A_2^\mu = 0.65$, $\tau_1^\mu = 2.0$ nsec, $\tau_2^\mu = 0.1$ nsec. The source is located at $(x_s, y_s) = (0.8, 0.34)$ m and the probe at $(x_p, y_p) = (0.78, 0.16)$ m.

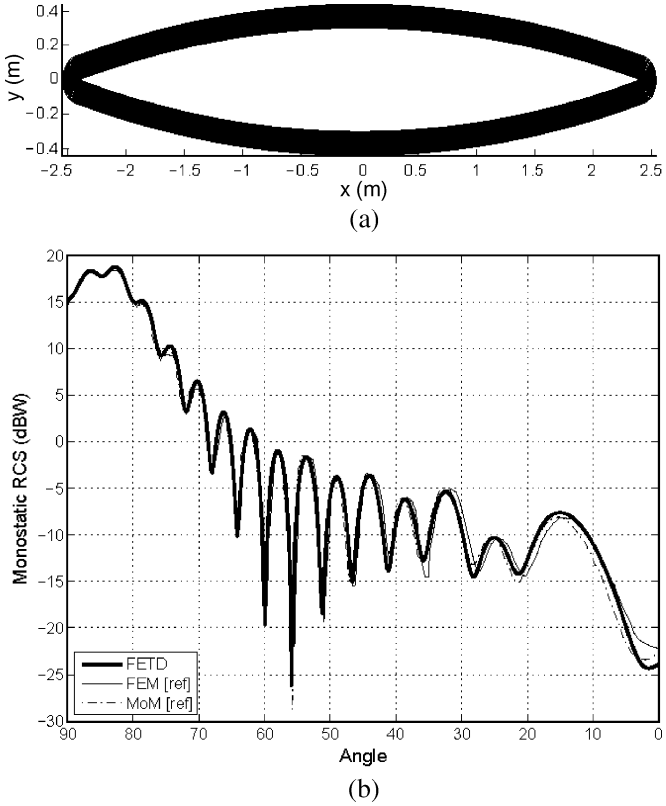

Fig. 6. (a) The finite element mesh used to calculate the monostatic RCS of the ogive cylinder has 103,367 edges and 67,881 faces. A Cartesian PML implementation for this problem would require a mesh about 2.3 times larger. (b) Monostatic RCS of the ogive with size $4\lambda_0 \times 1\lambda_0$ calculated by FETD, frequency-domain finite elements, and method of moments (MoM) [53].

Fig. 5(b) shows the scattered fields obtained by the conformal PML-FETD, compared to a reference FDTD result using Cartesian PML, showing very good agreement.

D. Monostatic-RCS: Ogive Cylinder

We next calculate the monostatic radar cross-section (RCS) of an ogive-shaped PEC object with a geometrical singularity as depicted in Fig. 6(a). The mesh shown in Fig. 6(a) has 103,367 edges and 67,881 faces. A mesh of similar density employing a Cartesian PML would require approximately 230,000 edges and 150,000 faces, more than twice the size of the mesh using the conformal PML. RCS calculations for similar geometries were studied using a Cartesian PML-FETD based on the second order wave equation in [29], [30].

For the RCS calculation, a plane-wave excitation is realized following a methodology similar to the plane-wave injection described in [51, pp. 201–212]. The scattered field is transformed to the frequency domain and the far-field is obtained by using a near- to far-field transformation. These operations are carried out at a contour in the tiled portion of the mesh that would normally separate different layers of the PML region. The PML stretching however, is offset by three layers in this case so that both the plane wave excitation and the near- to far-field transformation are done in the free-space region. The plane wave is injected through equivalent electric and magnetic source terms $\vec{J}_s(\vec{r}) = \hat{n} \times \vec{H}_i(\vec{r})$ and $\vec{M}_s(\vec{r}) = -\hat{n} \times \vec{E}_i(\vec{r})$, where $\hat{n}$ is the outward unit vector normal to the injection contour at $\vec{r}$. The

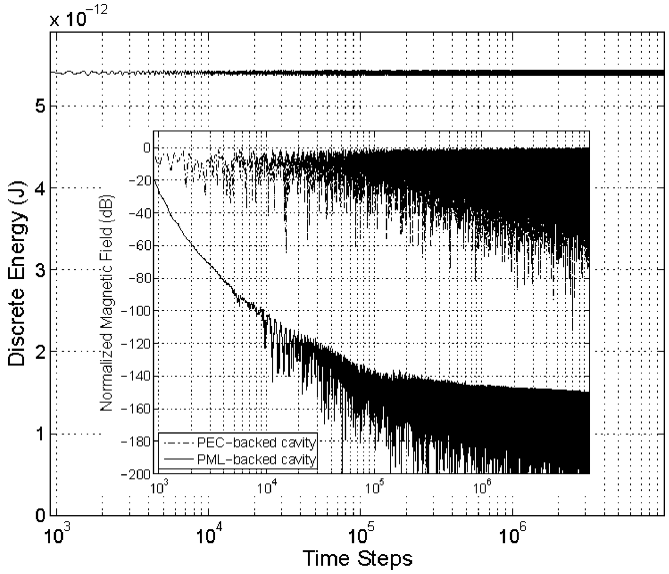

Fig. 7. The main plot shows the discrete energy for 10^7 time steps inside an oval shaped cavity terminated by PEC. The energy is constant except for small periodic fluctuations due to the leap-frog approximation in the time integration. This shows the energy-conserving property of the proposed method. The inset shows the normalized magnetic field magnitude in the PEC- and PML-backed cavity simulations, showing the late-time stability of the PML.

magnetic field vector associated with the plane-wave excitation is given in the time-domain by

$$\vec{H}_i(\vec{r},t) = \hat{z} f(t - t_0 - \hat{\beta}_i \cdot \vec{r}/v_c) \tag{31}$$

where $\hat{\beta}_i = \hat{x}\cos\varphi_i + \hat{y}\sin\varphi_i$ is the unit vector for incidence angle φ_i. The parameter t_0 is simply a time-offset for the FETD pulse excitation so that all fields in the computational domain are equal to zero for $t \leq 0$. The time-domain excitation $f(t)$ is again the Blackman-Harris pulse derivative. The contour comprised of edges that separate the tiled and non-tiled regions of the mesh (original PML boundary that is now offset by three layers) is used to insert the electric current source. The magnetic current source is applied at the two faces that touch each of these edges (with equal weights). The near- to far-field transformation is applied at a contour two cells away from the plane wave injection contour. in 2-D, the RCS is calculated using the following:

$$RCS(\varphi) = \frac{\left| \int\limits_{\mathcal{C}} \left[P(\vec{r'}) - Q(\vec{r'}) \right] e^{\jmath\beta\hat{r}\cdot\vec{r'}} dl' \right|^2}{4|\beta|\,|F(\omega)|^2} \tag{32}$$

with

$$P(\vec{r'}) = \beta\hat{z} \times \left(\hat{n} \times \vec{H}_s(\vec{r'}) \right) \cdot \hat{r} \tag{33}$$

$$Q(\vec{r'}) = \omega\epsilon_0 \hat{z} \cdot \left(\hat{n} \times \vec{E}_s(\vec{r'}) \right) \tag{34}$$

where $\beta = \omega/v_c$ is the wavenumber, $\mathcal{C}$ denotes the near-to-far field transformation contour, dl' is the infinitesimal arclength along $\mathcal{C}$, $\vec{E}_s(\vec{r'})$ and $\vec{H}_s(\vec{r'})$ are the frequency-domain scattered electric and magnetic fields evaluated along $\mathcal{C}$, $F(\omega)$ is the Fourier transform of $f(t)$, and $\hat{r} = \hat{x}\cos\varphi + \hat{y}\sin\varphi$ is the unit vector pointing towards the observation point. The lengths of the major and minor axes of the ogive are 8λ and 1λ, respectively. The average edge length of the finite element mesh is chosen as 0.015λ.

Fig. 6 shows the monostatic RCS calculated by the conformal PML-FETD, compared against frequency-domain finite element results and method of moments (MoM) results [53], showing again very good agreement.

E. Late-Time Stability and Energy Conservation

For a time-domain method based on a leap-frog update, there are necessary conditions on the matrices $[\mathcal{D}_{\text{curl}}]$, $[\mathcal{D}^*_{\text{curl}}]$, $[\star_\epsilon]$, and $[\star_{\mu^{-1}}]$ for (conditional) stability and energy conservation to hold, as discussed, e.g., in [54]. In order to numerically demonstrate late-time stability and energy conservation here, a scenario with the same domain boundary shape of Fig. 4(b) but scaled down four times (for faster update) is used (the average edge length is kept the same). The source is placed at $(x_s, y_s) = (0.1, 0.07)$ m and the magnetic field is probed at $(x_s, y_s) = (0.1, 0.13)$ m. Stability is tested by considering two different cases: (i) a cavity problem simulated by a mesh extruded by eight layers of free-space directly terminated by a PEC boundary, and (ii) a cavity problem simulated by the same mesh but where now the eight extruded layers constitute the PML. The total number of steps used in both cases is 10^7. The discrete energy is calculated by

$$\mathcal{W} = \mathbb{E}^T [\star_\epsilon] \mathbb{E} + \mathbb{B}^T [\star_{\mu^{-1}}] \mathbb{B}. \tag{35}$$

Fig. 7 shows the discrete energy with respect to time in the PEC-backed cavity problem where it is clearly seen that energy is conserved. Note that the increase in the oscillations is just an artifact of the logarithm scale chosen for the abscissa. The inset of Fig. 7 shows the time history of the magnetic field magnitude at the probe location. After 10^7 time steps, the magnetic field magnitude in the PML-backed case is about -150 dB down from that in the PEC-backed problem due to PML losses. The very small residual field value that remains is comprised of high-frequency components (with wavelength close to the average edge length) that are not well absorbed by the PML. No late-time instabilities or spurious linear growth [17], [18] are observed.

It should be pointed out that a conformal PML cannot be deployed over grid terminations having *convex* portions as viewed from inside the computational domain (i.e., with negative local radius of curvature under the present convention). In that case, the conformal PML would exhibit a dynamically *unstable* behavior. This is discussed in some detail elsewhere [43], [55].

V. Concluding Remarks

We have developed and implemented a conformal PML absorbing boundary condition for the FETD simulation of transient Maxwell equations in open-domain problems. The underlying FETD algorithm is based on a (mixed) expansion of the electric field in terms of edge elements and of the magnetic field in terms of face elements. The time discretization employs a leap-frog time update akin to FDTD except for a linear solve required for the electric field update.

The conformal PML produces significant computational savings by minimizing the buffer space in the computational grid around the scatterer(s). The accuracy and capabilities of the conformal PML-FETD have been demonstrated through several examples involving PEC scatterers and (doubly-)dispersive materials. The late-time stability and energy conservation properties of the method have also been verified numerically.

REFERENCES

[1] J. F. Lee, R. Lee, and A. Cangellaris, "Time-domain finite-element methods," *IEEE Trans. Antennas Propag.*, vol. 45, no. 3, pp. 430–442, 1997.

[2] A. Bossavit, *Computational Electromagnetics: Variational Formulations, Complementarity, Edge Currents*. San Diego, CA: Academic Press, 1998.

[3] J. Jin, *The Finite Element Method in Electromagnetics*. New York: Wiley, 2002.

[4] P. Monk, *Finite Element Methods for Maxwell's Equations*. Oxford, U.K.: Oxford Univ. Press, 2003.

[5] J.-F. Lee, "WETD-A finite element time-domain approach for solving Maxwell's equations," *IEEE Microw. Guided Wave Lett.*, vol. 4, no. 1, pp. 11–13, Jan. 1994.

[6] M. Feliziani and F. Maradei, "Hybrid finite element solution of time dependent Maxwell's curl equations," *IEEE Trans. Magn.*, vol. 31, no. 3, pp. 1330–1335, May 1995.

[7] M. Wong, O. Picon, and V. F. Hanna, "A finite element method based on Whitney forms to solve Maxwell equations in the time domain," *IEEE Tran. Magn.*, vol. 31, pp. 1618–1621, 1995.

[8] C. Thng, R. C. Booton, Jr., and K. C. Gupta, "FDTD-compatible edge-element, face-element time-domain method for electromagnetics," *Int. J. Microw. and Millim.-Wave Comp.-Aided Eng.*, vol. 6, no. 1, pp. 69–77, 1996.

[9] T. V. Yioultsis, N. V. Kantartzis, C. S. Antonopoulos, and T. D. Tsiboukis, "A fully explicit Whitney element—Time domain scheme with higher order vector finite elements for three-dimensional high frequency problems," *IEEE Trans. Magn.*, vol. 34, no. 5, pp. 3288–3291, Sep. 1998.

[10] J. Koning, R. N. Rieben, and G. H. Rodrigue, "Vector finite-element modeling of the full-wave Maxwell equations to evaluate power loss in bent optical fibers," *IEEE J. Lightw. Technol.*, vol. 23, no. 12, pp. 4147–4154, Dec. 2005.

[11] R. N. Rieben, G. H. Rodrigue, and D. A. White, "A high order mixed vector finite element method for solving the time dependent Maxwell equations on unstructured grids," *J. Comp. Phys.*, vol. 204, pp. 490–519, 2005.

[12] B. He and F. L. Teixeira, "A sparse and explicit FETD via approximate inverse Hodge (mass) matrix," *IEEE Microw. Wireless Compon. Lett.*, vol. 16, no. 6, pp. 348–350, Jun. 2006.

[13] A. Bossavit, "Mixed finite elements and the complex of Whitney forms," in *The Mathematics of Finite Elements and Applications VI*, J. R. Whiteman, Ed. London, U.K.: Academic Press, 1988, pp. 137–144.

[14] B. He and F. L. Teixeira, "Geometric finite element discretization of Maxwell equations in primal and dual spaces," *Phys. Lett. A*, vol. 349, pp. 1–14, 2006.

[15] B. He and F. L. Teixeira, "Differential forms, Galerkin duality, and sparse approximations in finite element solutions of Maxwell equations," *IEEE Trans. Antennas Propag.*, vol. 55, no. 5, pp. 1359–1368, 2007.

[16] B. He and F. L. Teixeira, "Mixed E-B finite elements for solving 1-D, 2-D, and 3-D time-harmonic Maxwell curl equations," *IEEE Microw. Wireless Comp. Lett.*, vol. 17, no. 5, pp. 313–315, 2007.

[17] S. Wang, R. Lee, and F. L. Teixeira, "Anisotropic-medium PML for vector FETD with modified basis functions," *IEEE Trans. Antennas Propag.*, vol. 54, no. 1, pp. 20–27, Jan. 2006.

[18] R. A. Chilton and R. Lee, "The discrete origin of FETD-Newmark late-time instability, and a correction scheme," *J. Comp. Phys.*, vol. 224, no. 2, pp. 1293–1306, 2007.

[19] R. Rieben, D. White, and G. Rodrigue, "High-order symplectic integration methods for finite element solutions to time dependent Maxwell equations," *IEEE Trans. Antennas Propag.*, vol. 52, no. 8, pp. 2190–2195, Aug. 2004.

[20] E. A. Forgy and W. C. Chew, "A time-domain method with isotropic dispersion and increased stability on an overlapped lattice," *IEEE Trans. Antennas Propag.*, vol. 50, no. 7, pp. 983–996, Jul. 2002.

[21] B. Donderici and F. L. Teixeira, "Mixed finite-element time-domain method for Maxwell equations in doubly dispersive media," *IEEE Trans. Microwave Theory Tech.*, vol. 56, no. 1, pp. 113–120, Jan. 2008.

[22] J. P. Berenger, "A perfectly matched layer for the absorption of electromagnetic waves," *J. Comput. Phys.*, vol. 114, no. 2, pp. 185–200, 1994.

[23] D. S. Katz, E. T. Thiele, and A. Taflove, "Validation and extension to three dimensions of the Berenger PML absorbing boundary condition," *IEEE Microw. Guided Wave Lett*, vol. 4, no. 8, pp. 268–270, 1994.

[24] W. C. Chew and W. Weedon, "A 3D perfectly matched medium from modified Maxwell's equations with stretched coordinates," *Microw. Opt. Tech. Lett.*, vol. 7, no. 13, pp. 599–604, 1994.

[25] Z. S. Sacks, D. M. Kingsland, R. Lee, and J.-F. Lee, "A perfectly matched anisotropic absorber for use as an absorbing boundary condition," *IEEE Trans. Antennas Propag.*, vol. 43, no. 12, pp. 1460–1463, 1995.

[26] S. D. Gedney, "The perfectly matched layer absorbing medium," in *Advances in Computational Electrodynamics: The Finite-Difference Time-Domain Method*, A. Taflove, Ed. Norwood, MA: Artech House, 1998, ch. 5, pp. 263–344.

[27] F. L. Teixeira, W. C. Chew, M. Straka, M. L. Oristaglio, and T. Wang, "Finite-difference time-domain simulation of ground penetrating radar on dispersive, inhomogeneous, and conductive media," *IEEE Trans. Geosci. Remote Sensing*, vol. 36, no. 6, pp. 1928–1937, 1998.

[28] D. Jiao, J.-M. Jin, E. Michielssen, and D. J. Riley, "Time-domain finite-element simulation of three-dimensional scattering and radiation problems using perfectly matched layers," *IEEE Trans. Antennas Propag.*, vol. 51, no. 2, pp. 296–305, Feb. 2003.

[29] T. Rylander and J.-M. Jin, "Perfectly matched layer for the time domain finite element method applied to Maxwell's equations," *J. Comp. Phys.*, vol. 200, pp. 238–250, May 2004.

[30] T. Rylander and J.-M. Jin, "Perfectly matched layer in three dimensions for the time-domain finite element method applied to radiation problems," *IEEE Trans. Antennas Propag.*, vol. 53, no. 4, pp. 1489–1499, Apr. 2005.

[31] E. A. Navarro, C. Wu, P. Y. Chung, and J. Litva, "Application of PML superabsorbing boundary condition to non-orthogonal FDTD method," *Electron. Lett.*, vol. 30, no. 20, pp. 1654–1655, 1994.

[32] J. A. Roden and S. D. Gedney, "Efficient implementation of the uniaxial-based PML media in three-dimensional nonorthogonal coordinates with the use of the FDTD technique," *Microw. Opt. Technol. Lett.*, vol. 14, no. 2, pp. 71–75, 1997.

[33] M. Kuzuoglu and R. Mittra, "Investigation of nonplanar perfectly matched absorbers for finite-element mesh truncation," *IEEE Trans. Antennas Propag.*, vol. 45, no. 3, Mar. 1997.

[34] F. L. Teixeira and W. C. Chew, "PML-FDTD in cylindrical and spherical grids," *IEEE Microw. Guided Wave Lett.*, vol. 7, no. 9, pp. 285–287, 1997.

[35] F. L. Teixeira and W. C. Chew, "Systematic derivation of anisotropic PML absorbing media in cylindrical and spherical coordinates," *IEEE Microw. Guided Wave Lett.*, vol. 7, no. 11, pp. 371–373, 1997.

[36] F. Collino and P. Monk, "The perfectly matched layer in curvilinear coordinates," *SIAM J. Sci. Computing*, vol. 19, pp. 2061–2090, 1998.

[37] F. L. Teixeira and W. C. Chew, "Finite-difference computation of transient electromagnetic fields for cylindrical geometries in complex media," *IEEE Trans. Geosci. Remote Sens.*, vol. 38, no. 4, pp. 1530–1543, 2000.

[38] P. G. Petropoulos, "Reflectionless sponge layers as absorbing boundary conditions for the numerical solution of Maxwell equations in rectangular, cylindrical and spherical coordinates," *SIAM J. Appl. Math.*, vol. 60, no. 3, pp. 1037–1058, 2000.

[39] F. L. Teixeira and W. C. Chew, "Analytical derivation of a conformal perfectly matched absorber for electromagnetic waves," *Microw. Opt. Tech. Lett.*, vol. 17, no. 4, pp. 231–236, 1998.

[40] F. L. Teixeira and W. C. Chew, "Differential forms, metrics, and the reflectionless absorption of electromagnetic waves," *J. Electromagn. Waves Appl.*, vol. 13, no. 5, pp. 665–686, 1999.

[41] F. L. Teixeira and W. C. Chew, "Complex space approach to perfectly matched layers: A review and some new developments," *Int. J. Numer. Model.*, vol. 13, pp. 441–455, 2000.

[42] K.-P. Hwang and J.-M. Jin, "Application of a hyperbolic grid generation technique to a conformal PML implementation," *IEEE Microw. Guided Wave Lett.*, vol. 9, no. 4, pp. 137–139, Apr. 1999.

[43] F. L. Teixeira, K.-P. Hwang, W. C. Chew, and J.-M. Jin, "Conformal PML-FDTD schemes for electromagnetic field simulations: A dynamic stability study," *IEEE Trans. Antennas Propag.*, vol. 49, no. 6, pp. 902–907, Jun. 2001.
[44] P. Liu, J.-D. Xu, and W. Wan, "A finite-element realization of a 3-D conformal PML," *Microw. Opt. Tech. Lett.*, vol. 30, no. 3, pp. 170–173, Aug. 2001.
[45] P. Liu and Y.-Q. Jin, "Numerical simulation of bistatic scattering from a target at low altitude above rough sea surface under an EM-wave incidence at low grazing angle by using the finite element method," *IEEE Trans. Antennas Propag.*, vol. 52, no. 5, pp. 1205–1210, May 2004.
[46] O. Ozgun and M. Kuzuoglu, "Locally-conformal perfectly matched layer implementation for finite element mesh truncation," *Microw. Opt. Tech. Lett.*, vol. 48, no. 9, pp. 1836–1839, Sep. 2006.
[47] O. Ozgun and M. Kuzuoglu, "Non-Maxwellian locally-conformal PML absorbers for finite element mesh truncation," *IEEE Trans. Antennas Propag.*, vol. 55, no. 3, pp. 931–937, Mar. 2007.
[48] T. Rylander and J.-M. Jin, "Conformal perfectly matched layers for the time domain finite element method," in *IEEE AP-S Int. Symp. Digest*, Jun. 2003, vol. 1, pp. 698–701.
[49] B. He and F. L. Teixeira, "On the degrees of freedom of lattice electrodynamics," *Phys. Lett. A*, vol. 336, no. 1, pp. 1–7, 2005.
[50] F. L. Teixeira and W. C. Chew, "Lattice electromagnetic theory from a topological viewpoint," *J. Math. Phys.*, vol. 40, no. 1, pp. 169–187, 1999.
[51] A. Taflove*, Computational Electrodynamics: The Finite Difference Time Domain*. Boston, MA: Artech House, 1995.
[52] C. A. Balanis*, Advanced Engineering Electromagnetics*. New York: Wiley, 1989.
[53] J.-M. Jin and N. Lu, "Finite element analysis of scattering using coupled basis functions for elliptic boundaries," *Proc. Inst. Elect. Eng. Microw. Antennas Propag.*, vol. 144, no. 6, pp. 501–508, Dec. 1997.
[54] S. Wang and F. L. Teixeira, "Some remarks on the stability of time-domain electromagnetic simulations," *IEEE Trans. Antennas Propag.*, vol. 52, no. 3, pp. 895–898, 2004.
[55] F. L. Teixeira and W. C. Chew, "On causality and dynamic stability of perfectly matched layers for FDTD simulations," *IEEE Trans. Microw. Theory Tech.*, vol. 47, no. 6, pp. 775–785, 1999.

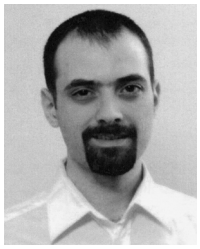

Burkay Donderici was born in Ankara, Turkey, in 1980. He received the B.S. degree from Bilkent University, Turkey, in 2002 and the M.S. degree from The Ohio State University, Columbus, in 2004, where he is currently working toward the Ph.D. degree.

Since 2002, he has been a Graduate Research Associate with the Electroscience Laboratory, The Ohio State University. During Summer 2007, he was with SciberQuest Inc., where he has worked on mesh stitching (subgridding) algorithms for electromagnetic particle-in-cell simulations. His research interests include computational electrodynamics and inverse scattering.

Fernando L. Teixeira (S'89–M'93–SM'05) received the B.S. and M.S. degrees from the Pontifical Catholic University of Rio de Janeiro, Brazil, in 1991 and 1995, respectively, and the Ph.D. degree from the University of Illinois at Urbana-Champaign, in 1999, all in electrical engineering.

From 1999 to 2000, he worked a Postdoctoral Research Associate with the Research Laboratory of Electronics, Massachusetts Institute of Technology. Since 2000, he has been with the Department of Electrical and Computer Engineering and the ElectroScience Laboratory, The Ohio State University, where he is now an Associate Professor. His current research interests include modeling of wave propagation, scattering, and transport phenomena for communications, sensing, and device applications. He has edited one book, and has authored over 70 journals papers.

Dr. Teixeira is a member of Commissions B and F of the of the International Union of Radio Science (URSI). He received many awards for his research, including the CAREER Award from NSF in 2004 and the triennial Henry Booker Fellowship from USNC/URSI in 2005.